Unveiling the critical role of interfacial ionic conductivity in all-solid-state lithium batteries

Changhong Wang [a], Jianwen Liang [a], Sooyeon Hwang [b], Xiaona Li [a], Yang Zhao [a], Keegan Adair [a], Changtai Zhao [a], Xia Li [a], Sixu Deng [a], Xiaoting Lin [a], Xiaofei Yang [a], Ruying Li [a], Huan Huang [c], Li Zhang [d], Shigang Lu [d], Dong Su [b,**], Xueliang Sun [a,*]

[a] Department of Mechanical and Materials Engineering, University of Western Ontario, 1151 Richmond St, London, Ontario, N6A 3K7, Canada
[b] Center for Functional Nanomaterials, Brookhaven National Laboratory, Upton, NY, 11973, United States
[c] Glabat Solid-State Battery Inc, 700 Collip Circle, London, ON, N6G 4X8, Canada
[d] China Automotive Battery Research Institute Co. Ltd, 5th Floor, No. 43, Mining Building, North Sanhuan Middle Road, Haidian District Beijing, P.C. 100088, China

ARTICLE INFO

ABSTRACT

Advancement of all-solid-state lithium-ion (Li$^+$) batteries (ASSLIBs) has been hindered by the large interfacial resistance mainly originating from interfacial reactions between oxide cathodes and solid-state sulfide electrolytes (SEs). To suppress the interfacial reactions, an interfacial coating layer between cathodes and SEs is indispensable. However, the kinetics of interfacial Li$^+$ transport across the coating layer has not been well understood yet. Herein, we tune the interfacial ionic conductivity of the coating layer LiNb$_{0.5}$Ta$_{0.5}$O$_3$ (LNTO) by manipulating post-annealing temperature. It is found that the interfacial ionic conductivity determines interfacial Li$^+$ transport kinetics and enhancing the interfacial ionic conductivity can significantly boost the electrochemical performance of SE-based ASSLIBs. A representative cathode LiNi$_{0.5}$Mn$_{0.3}$Co$_{0.2}$O$_2$ coated by LNTO with the highest interfacial ionic conductivity exhibits a high initial capacity of 152 mAh.g^{-1} at 0.1 C and 107.5 mAh.g^{-1} at 1 C. This work highlights the importance of increasing interfacial ionic conductivity for high-performance SE-based ASSLIBs.

1. Introduction

All-solid-state lithium-ion batteries (ASSLIBs) have gained worldwide attention in recent years due to their excellent safety feature and higher energy density over conventional LIBs with flammable liquid electrolytes [1–4]. However, the development of ASSLIBs has been hindered by several main challenges. The first challenge is the insufficient ionic conductivity of solid-state electrolytes [5]. which has been addressed by developing high Li$^+$-conductive solid-state sulfide electrolytes (SEs), such as Li$_{9.54}$Si$_{1.74}$P$_{1.44}$S$_{11.7}$Cl$_{0.3}$ (25 mS cm^{-1}) [6], Li$_7$P$_3$S$_{11}$ (17 mS cm^{-1}), Li$_{10}$GeP$_2$S$_{12}$ (12 mS cm^{-1}) [7], Li$_{10.35}$[Sn$_{0.27}$Si$_{1.08}$]P$_{1.65}$S$_{12}$ (11 mS cm^{-1}) [8], Li$_{6+x}$P$_{1-x}$Ge$_x$S$_5$I (18 mS cm^{-2}) [9], and Na$_{2.88}$Sb$_{0.88}$W$_{0.12}$S$_4$ (32 mS cm^{-1}) [10]. The second challenge is the large interfacial resistance between electrodes and SEs, which is mainly caused by undesirable interfacial reactions and poor interfacial solid-solid contact [11–15]. To improve the interfacial

solid-solid contact, soluble SEs in organic solvents (i.e. Li$_2$S–P$_2$S$_5$ [16], Li$_6$PS$_5$Cl [17], Li$_6$PS$_5$Br [18], LiI–LiSnS$_4$ [19], Na$_3$SbS$_4$ [20]) are developed to coat oxide cathodes, thus dramatically improving the solid-solid contact [21,22]. On the other hand, an interfacial coating layer (i.e. LiNbO$_3$ [23,24], Li$_4$Ti$_5$O$_{12}$ [25], Li$_2$O–ZrO$_2$ [26], or Li$_{0.35}$La$_{0.5}$Sr$_{0.05}$TiO$_3$ [27]) is required to suppress detrimental interfacial reactions between oxide cathodes and SEs [28–30]. However, the kinetics of interfacial Li$^+$ transport across the coating layer has not been well understood yet in SE-based ASSLIBs.

In this work, we purposely tuned the ionic conductivity of an interfacial coating layer LiNb$_{0.5}$Ta$_{0.5}$O$_3$ (LNTO) by manipulating postannealing temperature, aiming at investigating the effect of interfacial ionic conductivity on the electrochemical performance of SE-based ASSLIBs. It is found that the oxide cathode LiNi$_{0.5}$Mn$_{0.3}$Co$_{0.2}$O$_2$ (NMC532) coated with low Li$^+$-conductive LNTO interfacial layer exhibits a low Li$^+$ diffusivity of 1.11×10^{-11} cm^2 s^{-1}, while the NMC532

---

* Corresponding author.
** Corresponding author.
E-mail addresses: dsu@bnl.gov (D. Su), xsun9@uwo.ca (X. Sun).

coated with high Li$^+$-conductive LNTO shows a high Li$^+$ diffusivity of 1.36×10^{-10} cm^2 S^{-1}, suggesting that enhancing the interfacial ionic conductivity of the coating layer can significantly boost interfacial Li$^+$ diffusion kinetics in SE-based ASSLIBs. The high Li$^+$-conductive LNTO-coated NMC532 shows a high initial capacity of 152 mAh.g^{-1} at 0.1 C and 107.5 mAh.g^{-1} at 1C at room temperature. This work illustrates that enhancing interfacial ionic conductivity can significantly accelerate interfacial Li$^+$ transport kinetics, which is of great importance toward high-performance SE-based ASSLIBs.

2. Results and discussion

2.1. Synthesis of interfacial coating LiNb$_{0.5}$Ta$_{0.5}$O$_3$ (LNTO) with different ionic conductivity

LNTO has a low electrical conductivity (10^{-11} S cm^{-1}) and wide electrochemical window [30,31], which is beneficial for suppressing interfacial reactions at the cathode/SE interface and providing good interfacial stability upon cycling. Most interestingly, the ionic conductivity of LNTO can be tuned by altering post-annealing temperature [31–34], which provides us a unique platform for studying the effect of interfacial ionic conductivity of the coating layer on the electrochemical performance of SE-based ASSLIBs. Therefore, LNTO was synthesized by

a sol-gel method and annealed under different temperatures to obtain different ionic conductivities. First, thermogravimetry (TG) and differential scanning calorimetry (DSC) was employed to determine the annealing temperature of LNTO in air. As shown in TG-DSC curves (Fig. S1), the organic species of niobium (Nb) and tantalum (Ta) precursors are decomposed in the air before 350 °C. Three exothermic peaks are shown at 380 °C, 410 °C, and 427 °C, which implies the formation of LNTO nanocrystals [31,35]. No any exothermic peak is observed after 450 °C. Therefore, LNTO powder was determined to heat at 350 °C, 450 °C, and 550 °C in air for 2 h, respectively. The detailed experimental procedure can be found in Supporting Information. X-ray diffraction (XRD) patterns in Fig. 1a indicates that LNTO annealed at 350 °C, 450 °C and 550 °C is amorphous, partially crystallized, and fully crystallized, respectively. The ionic conductivities of LNTO annealed at 350 °C, 450 °C, and 550 °C are 13.2 μS cm^{-1}, 38.7 μS cm^{-1}, and 2.43 μS cm^{-1}, respectively, as determined by electrochemical impedance spectroscopy (EIS) (Fig. 1b and c). The EIS and XRD results demonstrate that polycrystalline and amorphous LNTO possess much higher ionic conductivity than the crystalline counterpart, which is fully consistent with that in early references. [31–33,35].

To interpose the LNTO with different ionic conductivities at the cathode/SE interface, LNTO sol-gel was coated on single-crystal NMC532 followed by the same post-annealing procedures. These
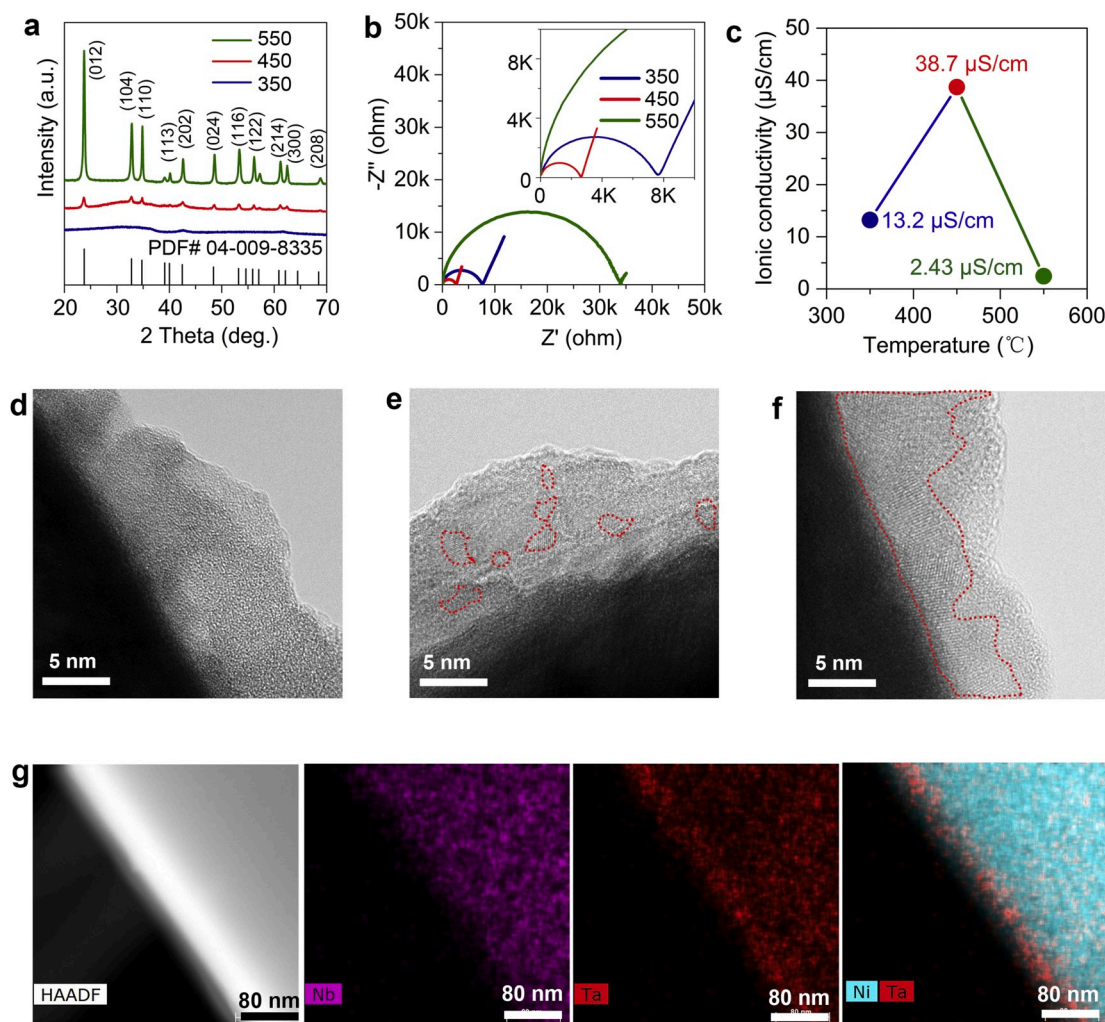

Fig. 1. Characterizations on LiNb$_{0.5}$Ta$_{0.5}$O$_3$ (LNTO) and LNTO@NMC532. (a) XRD patterns of LiNb$_{0.5}$Ta$_{0.5}$O$_3$ (LNTO) annealed at various temperatures. (b) EIS profile of LNTO after annealing at different temperatures. (c) The ionic conductivity of LNTO annealing at different temperatures. (d) A TEM image of LNTO@NMC532 annealed at 350 °C. (e) A TEM image of LNTO@NMC532 annealed at 450 °C. (f) A TEM image of LNTO@NMC532 annealed at 550 °C. (g) STEM-EDX mapping of Nb, Ta and Ni–Ta combination.

LNTO-coated NMC532 cathodes are labeled as LNTO@NMC532-350, LNTO@SC-NMC532-450, and LNTO@NMC532-550, respectively.

High-resolution transmission electron microscopy (HRTEM) was performed to inspect the crystallinity, thickness, and uniformity of the LNTO interfacial layer. Fig. 1d–f presents the HRTEM images of LNTO@NMC532-350, LNTO@NMC532-450, and LNTO@NMC532-550, respectively. The thickness of the interfacial LNTO layer is about 5–10 nm. Representative scanning TEM (STEM)-energy-dispersive X-ray (EDX) mapping of LNTO@NMC532-450 is present in Fig. 1g, verifying the uniformity and conformality of LNTO interfacial layer on NMC532 surface. The HRTEM image of LNTO@NMC532-350 shows no lattice fringes (Fig. 1d). Besides, no diffraction spots are detected in the electron diffraction pattern as shown in Fig. S2b, indicating that the interfacial LNTO layer annealed at 350 °C is amorphous. Based on the XRD and EIS results, the amorphous LNTO exhibits an ionic conductivity of 13.2 μS cm^{-1}. Comparatively, lots of nanocrystals are observed in the HRTEM image of LNTO@NMC532-450 (as highlighted by red circles in Fig. 1e). Moreover, the corresponding fast Fourier transform (FFT) pattern shows both discrete rings and diffraction spots (Fig. S2d), implying that the interfacial LNTO layer annealed at 450 °C is in a polycrystalline state. The polycrystalline LNTO exhibits a high ionic conductivity of 38.7 μS cm^{-1} according to the EIS and XRD results. More

interestingly, abundant lattice fringes are detected in the HRTEM images of LNTO@NMC532-550, as highlighted in Fig. 1f, which implies that the interfacial LNTO annealed at 550 is crystalline. The crystalline LNTO interfacial layer is also confirmed by the electron diffraction pattern in Fig. S2f. The crystalline LNTO interfacial layer demonstrates a low ionic conductivity of 2.43 μS cm^{-1} per EIS and XRD result. Combining TEM observation with XRD and EIS analyses, it is convinced that the interfacial LNTO coating with different ionic conductivities was successfully established on oxide cathode NMC532.

To ensure that all the NMC532 particles are fully covered by the interfacial LNTO coating layer, scanning electron microscopy (SEM) coupled with EDX was performed at the micrometer scale. As displayed in Figs. S3, S4, and S5, the uniform distribution of Nb and Ta on all the NMC532 particles confirm that all NMC532 particles are fully coated by LNTO. Fig. S6 shows the XRD patterns of LNTO@NMC532 after annealing under different temperatures. The unchanged (003) peaks suggest that interfacial coating LNTO does not diffuse into the NMC532 lattice during the annealing process. The same thickness, same chemical composition, and full coverage of LNTO on NMC532 particles serve as a reliable foundation for investigating the role of interfacial ionic conductivity in SE-based ASSLIBs.
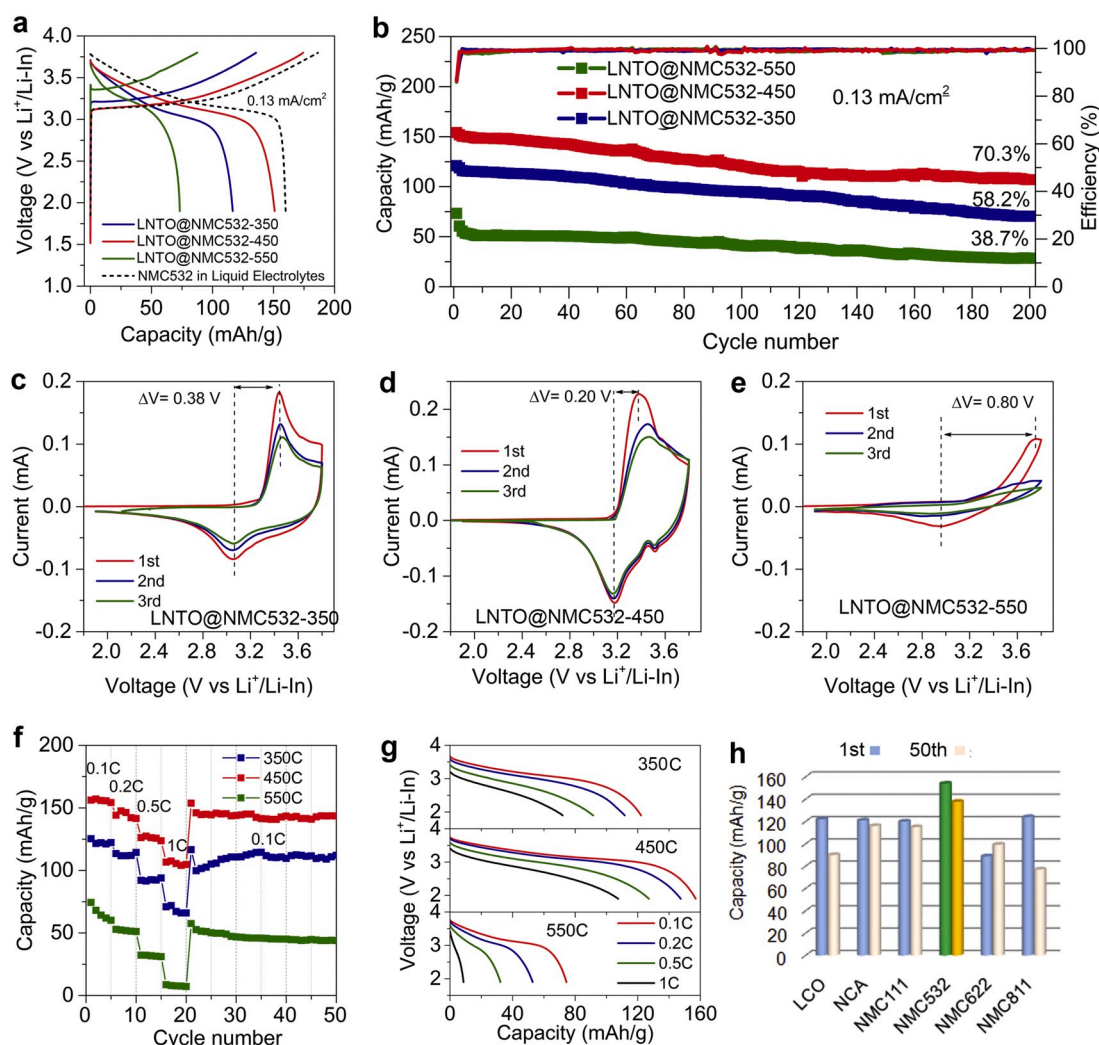

Fig. 2. Electrochemical performance of LNTO@SC-NMC532-based ASSLIBs. (a) The comparison of the charge-discharge curves of LNTO@NMC532-350, LNTO@NMC532-450, and LNTO@NMC532-550. (b) The cycling stability and coulombic efficiency of LNTO@NMC532-350, LNTO@NMC532-450, and LNTO@NMC532-550. (c) CV profiles of LNTO@NMC532-350. (d) CV profiles of LNTO@NMC532-450. (e) CV profiles of LNTO@NMC532-550. (f) Rate performance of LNTO@NMC532-350, LNTO@NMC532-450, and LNTO@NMC532-550. (g) Discharge curves with different current densities of LNTO@NMC532-350, LNTO@NMC532-450, and LNTO@NMC532-550. (h) The comparison of electrochemical performance with previous results related to SE-based ASSLIBs.

2.2. Electrochemical performance of LNTO@NMC532-based ASSLIBs

To fairly evaluate the electrochemical performance of these three cathodes in SE-based ASSLIBs, typical $Li_{10}GeP_2S_{12}$ (LGPS) was selected as the solid-state electrolyte due to its high ionic conductivity of (2.8 mS cm^{-1}) [36]. Fig. 2a shows their initial charge/discharge curves at a current density of 130 μA cm^{-2} (0.1 C). The initial de-lithiation voltage (3.25 V vs Li$^+$/Li–In) and polarization of LNTO@NMC532-450 are discernibly smaller than those of the other two cathodes. At the initial stage of charging, the initial de-lithiation voltage of LNTO@NMC532-450 overlaps with that of NMC532-based liquid cells at the same current density, suggesting that highly Li$^+$-conductive LNTO interfacial layer can enable the interfacial Li$^+$ transport as fast as that in liquid cells. The initial discharge curve of LNTO@NMC532 is slightly lower than that of liquid cells, which is probably due to the volume change-induced physical contact loss between NMC532 and LGPS, as revealed in previous work [37,38].

The initial discharge capacity of LNTO@NMC532-450 is 152 mAh. g^{-1}, higher than those of LNTO@NMC532-350 (120.9 mAh.g^{-1}) and LNTO@NMC532-550 (73.2 mAh.g^{-1}). The initial Coulombic efficiency of LNTO@NMC532-350, LNTO@NMC532-450, and LNTO@NMC532-550 is 87.14%, 86.68%, and 85.98%, respectively, which are close to that of NMC532-based liquid cells (85.79%) (Fig. S7). The high initial Coulombic efficiency of three cathodes hints that interfacial reactions between NMC532 and LGPS have been fully suppressed by the interfacial LNTO coating. The capacity retention after 200 cycles of LNTO@NMC532-350, LNTO@NMC-532-450, and LNTO@NMC532-550 is around 58.2%, 70.3%, and 38.7%, respectively (Fig. 2b). The average Coulombic efficiency of LNTO@NMC532-450 is 99.2% after the second cycle.

Furthermore, cyclic voltammetry (CV) curves of LNTO@NMC532-350, LNTO@NMC532-450, and LNTO@NMC532-550 were compared in Fig. 2c, d, and 2e, respectively. It can be seen that the oxidation/reduction peak currents of LNTO@NMC532-450 and LNTO@NMC532-350 are larger than that of LNTO@NMC532-550, which is consistent with their higher initial discharge capacity. Also, the polarization voltage (0.20 V) between oxidization and reduction peaks of LNTO@NMC532-450 is much smaller than those of LNTO@NMC532-350 (0.38 V) and LNTO@NMC532-550 (0.80 V), further verifying that LNTO@NMC532-450 possesses the best reversibility and the fastest Li$^+$ transport kinetics.

The rate-performance of LNTO@NMC532-350, LNTO@NMC532-450, and LNTO@NMC532-550 were also compared (Fig. 2f) and their corresponding curves at 0.1 C, 0.2 C, 0.5 C, and 1 C are present in Fig. 2g. Remarkably, the LNTO@NMC532-450 demonstrates the best rate performance. Even at 1 C, the specific capacity keeps at 107.5 mAh.g^{-1}. In contrast, the LNTO@NMC532-550 displays the capacity of 8.6 mAh.g^{-1} at 1 C. Comparing the best electrochemical performance of LNTO@NMC-532-450 with those previously reported electrochemical performances of SE-based ASSLIBs [9,38–41], both the specific capacity and capacity retention outperforms most of the previously reported

results (Fig. 2h) (Table S1).

To ensure that the electrochemical performance difference is truly originated from the different interfacial ionic conductivity of LNTO coating layer, not caused by interfacial reactions between NMC532 and LGPS, EIS was conducted to examine the interfacial resistance change during the initial charge process, upon which most of the interfacial reactions occur [38,42]. Fig. 3a, b, and 3c present the EIS profiles of LNTO@NMC532-based ASSLIBs being charged to various cut-off voltages from 3.3 V to 3.8 V. The negligible change of EIS profiles from 3.3 V to 3.8 V strongly demonstrates that the interfacial reactions between NMC532 and LGPS are successfully suppressed. All the EIS profiles mainly consist of two semi-circles except for the first EIS profile (a slope) of LNTO@NMC532-550 charging to 3.3 V. The slope is caused by the large polarization that retards the de-lithiation process of LNTO@NMC532-550 even being charged to 3.3 V. As simulated by the equivalent circuits inserted in Fig. S8(d) [23], the inception is related to the resistance of solid electrolytes layer, the semi-circle at the high-frequency region is related to the interfacial resistance between NMC532 and LGPS and grain boundary resistance of LGPS, while the low-frequency semicircle represents the anode interfacial resistance (Fig. S8) [38,43]. Among them, LNTO@NMC532-450 exhibits the smallest interfacial resistance (124 Ω), while LNTO@NMC532-350 and LNTO@NMC532-550 show relatively larger interfacial resistance of 369 Ω and 672 Ω, respectively. By relating the interfacial resistance with interfacial ionic conductivity, it is conceivable confirming that the LNTO buffer layer with higher interfacial ionic conductivity is beneficial for interfacial Li$^+$ transport.

Furthermore, the interfacial resistances of these cathodes were analyzed after 100 cycles. Compared to the first cycle, the interfacial resistance after 100 cycles is increased to 170 Ω, 402 Ω, and 800 Ω, respectively, indicating that there is some degradation of LGPS after long-term electrochemical cycling. Furthermore, HR-TEM was employed to probe the interface change after electrochemical cycling. Representatively, Fig. S10 presents the HR-TEM images of LNTO@NMC532-450 cathodes after 100 cycles, clearly showing that a 50–70 nm interfacial layer consisting of P and S species sitting on the LNTO@NMC532 surface. The TEM observation is consistent with EIS analysis.

2.3. Quantifying Li$^+$ diffusion coefficient of LNTO@NMC532

Galvanostatic intermittent titration technique (GITT) was further performed to quantify Li$^+$ diffusivity of LNTO@NMC532 cathodes, because an interfacial coating layer has a profound impact on the Li$^+$ diffusivity of electrode materials, as widely studied in liquid cells [44–51]. Fig. 4a displays the typical discharging GITT curves of the LNTO@NMC532-350, LNTO@NMC532-450, and LNTO@NMC532-550 at 0.1 C. Obviously, LNTO@NMC532-450 shows the lowest polarization among them, indicating the fastest Li$^+$ kinetics [46]. Besides, the voltage drop (IR$_{drop}$) after the current interruption is closely related to the Li$^+$ transport resistance inside the solid-state batteries. Typically, the IR$_{drop}$
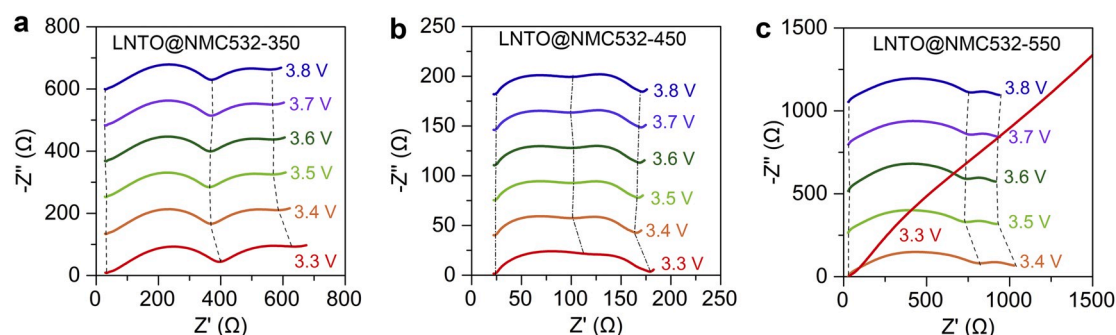

Fig. 3. EIS profiles of ASSLIBs being charged at different cut-off voltages. (a) LNTO@NMC532-350, (b) LNTO@NMC532-450, (c) LNTO@NMC532-550.
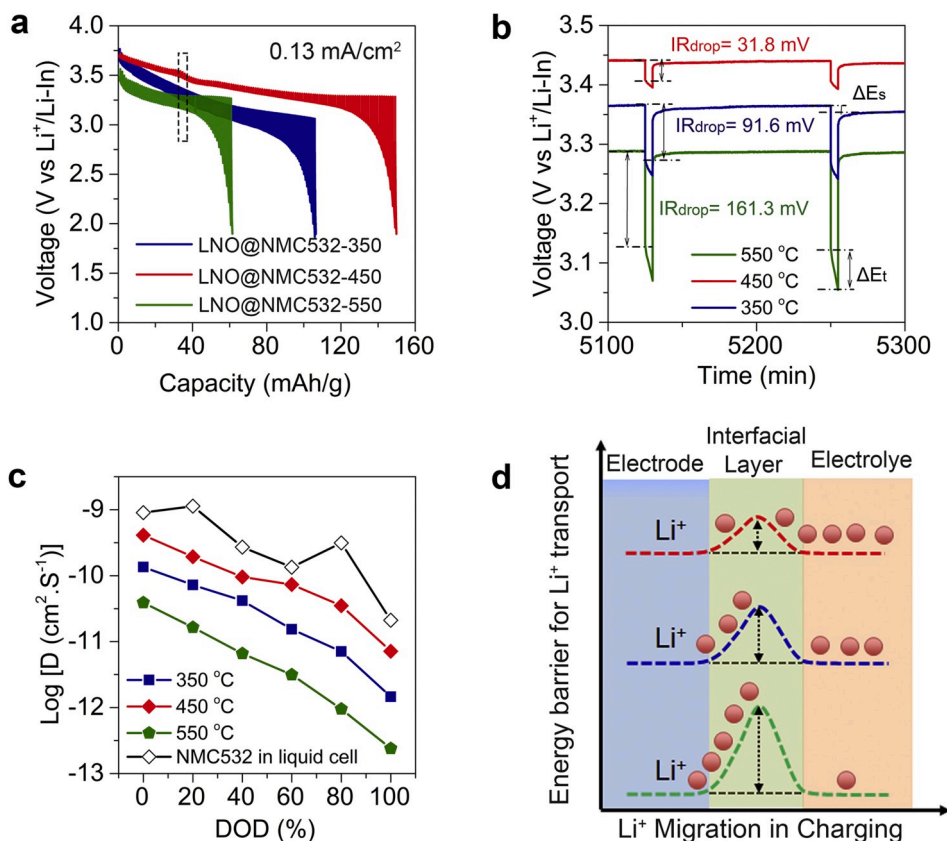
Fig. 4. Analysis of Li$^+$ transport kinetics. (a) Initial discharging GITT profiles of LNTO@NMC532-350, LNTO@NMC532-450, and LNTO@NMC532-550. (b) Typical GITT curves marked with IR drop, (c) Li$^+$ diffusion coefficient of LNTO@NMC532-350, LNTO@NMC532-450, and LNTO@NMC532-550 as a function of the depth of discharge (DOD). (d) Schematics of Li$^+$ transport across the electrode-electrolyte interface with different energy barriers.

of LNTO@SC-NMC532-450 is only 31.8 mV (Fig. 4b), which is approximately 3 times lower than that of LNTO@SC-NMC532-450 (91.6 mV) and 5 times lower than that of LNTO@SC-NMC532-450 (161.3 mV). The Li$^+$ diffusivity of these LNTO@NMC532 electrodes can be quantitatively calculated according to the equation [45].

$$D_{Li^+} = \frac{4}{\pi\tau} \left(\frac{m_{NMC532}V_{NMC532}}{M_{NMC532}S}\right)^2 \left(\frac{\Delta E_s}{\Delta E_\tau}\right)^2 \tag{1}$$

where τ is the relaxation time (2 h), m_{NMC532} is the mass of SC-NMC532 in the electrode composite. V_{NMC532} is the molar volume of SC-NMC532 (20.73 cm^3 mol^{-1}), M_{NMC532} is the molar mass of host materials, for the discharge process, the host material is SC-Li$_{0.3}$(Ni$_{0.5}$Mn$_{0.3}$Co$_{0.2}$)O$_2$ (91.66 g mol^{-1}). ΔE_s is the steady-voltage change after 2 h of relaxation. ΔE_τ is the change in the transient-voltage change after 5 min discharge process at 0.13 mA cm^{-2} ΔE_s and ΔE_τ were illustrated in Fig. 4b.

Fig. 4c compares the Li$^+$ diffusivity of LNTO@NMC532−350, LNTO@NMC532−450, and LNTO@NMC532−550 as a function of the different depth of discharge (DOD). In general, the Li$^+$ diffusion coefficient decreases with the increase of DOD, which is accompanied by the saturation of Li$^+$ sites in NMC532 upon the discharge, thus the Li$^+$ concentration gradient gradually decreases upon discharge [48,50]. Comparatively, the average Li$^+$ diffusivity of LNTO@NMC532−350, LNTO@NMC532−450, and LNTO@NMC532−550 in ASSLIBs are 4.55 × 10^{-11} cm [2].s^{-1}, 1.36 × 10^{-10} cm [2].s^{-1}, and 1.11 × 10^{-11} cm [2]. s^{-1}, respectively, which are lower than that of liquid cells (4.62 × 10^{-10} cm [2].s^{-1}) (Fig. S11), indicating that the coating layer slows down the Li$^+$ transport in solid-state batteries. However, the Li$^+$ diffusivity of LNTO@NMC532-450 and LNTO@NMC532-350 are approximately 12 and 4 times faster than that of LNTO@NMC532-550, demonstrating that enhancing the interfacial ionic conductivity of a coating layer can

significantly boost the Li$^+$ transport kinetics in solid-state batteries. The GITT analysis demonstrates that high Li$^+$-conductive LNTO coated NMC532 exhibits fast Li$^+$ diffusion kinetics while low Li$^+$-conductive LNTO coated NMC532 manifests sluggish Li$^+$ diffusion kinetics in solid-state batteries. Therefore, enhancing the interfacial ionic conductivity of a coating layer can significantly accelerate the interfacial Li$^+$ transport kinetics, thus advancing the electrochemical performance of SE-based ASSLIBs.

Fig. 4d illustrates Li$^+$ transport across the interfacial coating with different energy barriers. The high interfacial ionic conductivity of the interfacial layer can conduct Li$^+$ fast across the interface, which is corresponding to a low energy barrier for interfacial Li$^+$ transport. In contrast, the low interfacial ionic conductivity of the interfacial layer conducts Li$^+$ very slow, thus showing a high energy barrier for interfacial Li$^+$ transport. A detailed and in-depth discussion about the Li$^+$ transport process in a solid-state battery can be found in Fig. S12.

3. Conclusions

In summary, we manipulated the ionic conductivity of the interfacial coating layer by tuning post-annealing temperature and investigated its effect interfacial ionic conductivity on the electrochemical performance of SE-based ASSLIBs for the first time. It is found that the interfacial ionic conductivity of a coating layer determines the interfacial Li$^+$ transport kinetics and enhancing the interfacial ionic conductivity of the coating layer can significantly accelerate the interfacial Li$^+$ transport, which in turn boost the electrochemical performance of SE-based ASSLIBs. The oxide cathode NMC532 coated with the highest Li$^+$-conductive LNTO exhibits the highest Li$^+$ diffusion coefficient of 1.36 × 10^{-10} cm [2].s^{-1}. Resultantly, the LNO@NMC532 demonstrates a high capacity of 152 mAh.g^{-1} at 0.1 C and 107.5 mAh.g^{-1} at 1 C. This work suggests that

enhancing the interfacial ionic conductivity is crucial for high-performance SE-based ASSLIBs.

Declaration of competing interest

The authors declare that they have no known competing financial interests or personal relationships that could have appeared to influence the work reported in this paper.

CRediT authorship contribution statement

Changhong Wang: Writing - original draft. **Jianwen Liang:** Formal analysis. **Sooyeon Hwang:** Investigation, Methodology. **Xiaona Li:** Formal analysis. **Yang Zhao:** Formal analysis. **Keegan Adair:** Writing - review & editing. **Changtai Zhao:** Methodology. **Xia Li:** Formal analysis. **Sixu Deng:** Formal analysis. **Xiaoting Lin:** Formal analysis. **Xiaofei Yang:** Formal analysis. **Ruying Li:** Resources. **Huan Huang:** Project administration. **Li Zhang:** Project administration. **Shigang Lu:** Project administration. **Dong Su:** Supervision. **Xueliang Sun:** Supervision.

Acknowledgments

Appendix A. dSupplementary data

Supplementary data to this article can be found online at https://doi.org/10.1016/j.nanoen.2020.104686.

References

[1] S. Xia, X. Wu, Z. Zhang, Y. Cui, W. Liu, Inside Chem. (2019) 1–33, https://doi.org/10.1016/j.chempr.2018.11.013.

[2] X.-B. Cheng, C.-Z. Zhao, Y.-X. Yao, H. Liu, Q. Zhang, Inside Chem. 5 (2019) 74–96.

[3] Y. Zhao, K. Zheng, X. Sun, Joule (2018) 1–22.

[4] M.B. Dixit, W. Zaman, N. Hortance, S. Vujic, B. Harkey, F. Shen, W.-Y. Tsai, V. De Andrade, X.C. Chen, N. Balke, K.B. Hatzell, Joule 4 (2020) 207–221.

[5] A. Miura, N.C. Rosero-Navarro, A. Sakuda, K. Tadanaga, N.H.H. Phuc, A. Matsuda, N. Machida, A. Hayashi, M. Tatsumisago, Nat. Rev. Chem. 3 (2019) 189–198.

[6] Y. Kato, S. Hori, T. Saito, K. Suzuki, M. Hirayama, A. Mitsui, M. Yonemura, H. Iba, R. Kanno, Nat. Energy 1 (2016) 16030.

[7] N. Kamaya, K. Homma, Y. Yamakawa, M. Hirayama, R. Kanno, M. Yonemura, T. Kamiyama, Y. Kato, S. Hama, K. Kawamoto, A. Mitsui, Nat. Mater. 10 (2011) 682–686.

[8] Y. Sun, K. Suzuki, S. Hori, M. Hirayama, R. Kanno, Chem. Mater. 29 (2017) 5858–5864.

[9] M.A. Kraft, S. Ohno, T. Zinkevich, R. Koerver, S.P. Culver, T. Fuchs, A. Senyshyn, S. Indris, B.J. Morgan, W.G. Zeier, J. Am. Chem. Soc. 140 (2018) 16330–16339.

[10] A. Hayashi, N. Masuzawa, S. Yubuchi, F. Tsuji, C. Hotehama, A. Sakuda, M. Tatsumisago, Nat. Commun. 10 (2019) 5266.

[11] H. Lee, P. Oh, J. Kim, H. Cha, S. Chae, S. Lee, J. Cho, Adv. Mater. 31 (2019) 1900376.

[12] S.P. Culver, R. Koerver, W.G. Zeier, J. Janek, Adv. Energy Mater. 9 (2019) 1900626.

[13] P.K. Ho, B. Qiang, K.D. Hyeon, O.D. Yang, Z. Yizhou, M. Yifei, J.Y. Seok, Adv. Energy Mater. (2018) 1800035, 0.

[14] X. Fan, X. Ji, F. Han, J. Yue, J. Chen, L. Chen, T. Deng, J. Jiang, C. Wang, Sci. Adv. 4 (2018) 9245.

[15] X. Li, J. Liang, X. Li, C. Wang, J. Luo, R. Li, X. Sun, Energy Environ. Sci. 11 (2018) 2828.

[16] S. Teragawa, K. Aso, K. Tadanaga, A. Hayashi, M. Tatsumisago, J. Power Sources 248 (2014) 939–942.

[17] D.H. Kim, D.Y. Oh, K.H. Park, Y.E. Choi, Y.J. Nam, H.A. Lee, S.-M. Lee, Y.S. Jung, Nano Lett. 17 (2017) 3013–3020.

[18] S. Yubuchi, M. Uematsu, C. Hotehama, A. Sakuda, A. Hayashi, M. Tatsumisago, J. Mater. Chem. 7 (2019) 558–566.

[19] K.H. Park, D.Y. Oh, Y.E. Choi, Y.J. Nam, L. Han, J.-Y. Kim, H. Xin, F. Lin, S.M. Oh, Y.S. Jung, Adv. Mater. 28 (2016) 1874–1883.

[20] A. Banerjee, K.H. Park, J.W. Heo, Y.J. Nam, C.K. Moon, S.M. Oh, S.-T. Hong, Y.S. Jung, Angew. Chem. Int. Ed. 55 (2016) 9634–9638.

[21] K.H. Park, Q. Bai, D.H. Kim, D.Y. Oh, Y. Zhu, Y. Mo, Y.S. Jung, Adv. Energy Mater. 8 (2018) 1800035.

[22] S. Yubuchi, M. Uematsu, M. Deguchi, A. Hayashi, M. Tatsumisago, ACS Appl. Energy Mater. 1 (2018) 3622–3629.

[23] N. Ohta, K. Takada, L. Sakaguchi, L. Zhang, R. Ma, K. Fukuda, M. Osada, T. Sasaki, Electrochem. Commun. 9 (2007) 1486–1490.

[24] C. Wang, X. Li, Y. Zhao, M.N. Banis, J. Liang, X. Li, Y. Sun, K.R. Adair, Q. Sun, Y. Liu, F. Zhao, S. Deng, X. Lin, R. Li, Y. Hu, T.-K. Sham, H. Huang, L. Zhang, R. Yang, S. Lu, X. Sun, Small Methods (2019) 1900261, https://doi.org/10.1002/smtd.201900261.

[25] N. Ohta, K. Takada, L. Zhang, R. Ma, M. Osada, T. Sasaki, Adv. Mater. 18 (2006) 2226–2229.

[26] T. Shi, Q. Tu, Y. Tian, Y. Xiao, L.J. Miara, O. Kononova, G. Ceder, Advanced Energy Materials, n/a, 2019, p. 1902881.

[27] D. Cao, Y. Zhang, A.M. Nolan, X. Sun, C. Liu, J. Sheng, Y. Mo, Y. Wang, H. Zhu, Nano Lett. (2019), https://doi.org/10.1021/acs.nanolett.1029b02678. DOI: 10.1021/acs.nanolett.9b02678.

[28] S.P. Culver, R. Koerver, W.G. Zeier, J. Janek, Adv. Energy Mater. (2019) 1900626, 0.

[29] Y. Xiao, L.J. Miara, Y. Wang, G. Ceder, Joule (2019), https://doi.org/10.1016/j.joule.2019.02.006.

[30] Y. Zhu, X. He, Y. Mo, J. Mater. Chem. 4 (2016) 3253–3266.

[31] A.M. Glass, K. Nassau, T.J. Negran, J. Appl. Phys. 49 (1978) 4808–4811.

[32] H. Aono, N. Imanaka, G.-y. Adachi, Acc. Chem. Res. 27 (1994) 265–270.

[33] S. Lanfredi, A.C.M. Rodrigues, J. Appl. Phys. 86 (1999) 2215–2219.

[34] C. Yada, C.E. Lee, D. Laughman, L. Hannah, H. Iba, B.E. Hayden, J. Electrochem. Soc. 162 (2015) A722–A726.

[35] N. Özer, C.M. Lampert, Sol. Energy Mater. Sol. Cells 39 (1995) 367–375.

[36] C. Wang, K.R. Adair, J. Liang, X. Li, Y. Sun, X. Li, J. Wang, Q. Sun, F. Zhao, X. Lin, R. Li, H. Huang, L. Zhang, R. Yang, S. Lu, X. Sun, Adv. Funct. Mater. (2019) 1900392, https://doi.org/10.1002/adfm.201900392.

[37] R. Koerver, W. Zhang, L. de Biasi, S. Schweidler, A.O. Kondrakov, S. Kolling, T. Brezesinski, P. Hartmann, W.G. Zeier, J. Janek, Energy Environ. Sci. (2018), https://doi.org/10.1039/C8EE00907D.

[38] R. Koerver, I. Aygün, T. Leichtweiß, C. Dietrich, W. Zhang, J.O. Binder, P. Hartmann, W.G. Zeier, J. Janek, Chem. Mater. 19 (2017) 5574–5582.

[39] A. Sakuda, H. Kitaura, A. Hayashi, M. Tatsumisago, Y. Hosoda, T. Nagakane, A. Sakamoto, Chem. Lett. 41 (2012) 260–261.

[40] S. Ito, S. Fujiki, T. Yamada, Y. Aihara, Y. Park, T.Y. Kim, S.-W. Baek, J.-M. Lee, S. Doo, N. Machida, J. Power Sources 248 (2014) 943–950.

[41] N. Machida, J. Kashiwagi, M. Naito, T. Shigematsu, Solid State Ionics 225 (2012) 354–358.

[42] K. Takada, N. Ohta, L. Zhang, K. Fukuda, I. Sakaguchi, R. Ma, M. Osada, T. Sasaki, Solid State Ionics 179 (2008) 1333–1337.

[43] A.Y. Kim, F. Strauss, T. Bartsch, J.H. Teo, T. Hatsukade, A. Mazilkin, J. Janek, P. Hartmann, T. Brezesinski, Chem. Mater. (2019), https://doi.org/10.1021/acs.chemmater.9b02947.

[44] X.H. Rui, N. Yesibolati, S.R. Li, C.C. Yuan, C.H. Chen, Solid State Ionics 187 (2011) 58–63.

[45] X.H. Rui, N. Ding, J. Liu, C. Li, C.H. Chen, Electrochim. Acta 55 (2010) 2384–2390.

[46] J. Li, X. Xiao, Y.-T. Cheng, M.W. Verbrugge, J. Phys. Chem. Lett. 4 (2013) 3387–3391.

[47] S. Shi, P. Lu, Z. Liu, Y. Qi, L.G. Hector, H. Li, S.J. Harris, J. Am. Chem. Soc. 134 (2012) 15476–15487.

[48] R. Amin, Y.-M. Chiang, J. Electrochem. Soc. 163 (2016) A1512–A1517.

[49] J.S. Park, A.U. Mane, J.W. Elam, J.R. Croy, ACS Omega 2 (2017) 3724–3729.

[50] Y.J. Kim, H. Kim, B. Kim, D. Ahn, J.-G. Lee, T.-J. Kim, D. Son, J. Cho, Y.-W. Kim, B. Park, Chem. Mater. 15 (2003) 1505–1511.

[51] J.-Y. Liang, X.-X. Zeng, X.-D. Zhang, P.-F. Wang, J.-Y. Ma, Y.-X. Yin, X.-W. Wu, Y.-G. Guo, L.-J. Wan, J. Am. Chem. Soc. 140 (2018) 6767–6770.